

# A new control volume finite element method for the stable and accurate solution of the drift-diffusion equations on general unstructured grids.

Pavel Bochev<sup>\*†</sup> and Kara Peterson

*Numerical Analysis and Applications, MS1320, Sandia National Laboratories,  
P.O. Box 5800, Albuquerque, New Mexico 87185*

## SUMMARY

We present a new Control Volume Finite Element Method (CVFEM) for the drift-diffusion equations. The method combines a conservative formulation of the current continuity equations with a novel definition of an exponentially fitted elemental current density. An edge element representation of the nodal CVFEM current density in the diffusive limit motivates this definition. We prove that in the absence of carrier drift the nodal current is sum of edge currents, which solve one-dimensional diffusion problems, times  $H(\text{curl})$ -conforming edge basis functions. Replacement of the edge diffusion problems by one-dimensional drift-diffusion equations extends this representation to the general case. The resulting  $H(\text{curl}, \Omega)$ -conforming, exponentially fitted current (EFC) density field combines the upwind effect from all edges and enables accurate computation of current density integrals on arbitrary surfaces inside the elements. This obviates the need for the control volumes to be topologically dual to the finite elements and results in a method that is stable and accurate on general unstructured finite element grids. This sets apart our approach from other schemes, such as the Scharfetter-Gummel Box Integration Method, which require topologically dual grids. Numerical studies of the CVFEM-EFC for a suite of standard advection-diffusion test problems on nonuniform grids confirms the accuracy and the robustness of the new formulation. Simulation of an n-channel MOSFET device tests the method in a more realistic setting. Copyright © 2012 John Wiley & Sons, Ltd.

Received ...

**KEY WORDS:** Control Volume Finite Element method, edge elements, exact sequence, compatible finite elements, drift-diffusion equations, device modeling, Scharfetter-Gummel method, topologically dual grids

## 1. INTRODUCTION

The drift-diffusion equations are a coupled system of nonlinear Partial Differential Equations (PDE's) [21, 19], which model the motion of electrons and holes in semiconductor materials. Predictive simulation of semiconductor devices depends on the robust, accurate and efficient numerical solution of these equations. Two desirable properties of numerical schemes for the drift-diffusion equations are (a) stability in the advection-dominated regime, i.e., when charge drift velocities dominate their diffusivity, and (b) local conservation of electron and hole current densities.

A standard approach for stabilization of advection-dominated problems is to introduce additional dissipation into the numerical scheme through artificial diffusion, upwinding or exponential fitting.

<sup>\*</sup>Correspondence to: Numerical Analysis and Applications, MS1320, Sandia National Laboratories, P.O. Box 5800, Albuquerque, New Mexico 87185

<sup>†</sup>Sandia National Laboratories is a multi-program laboratory managed and operated by Sandia Corporation, a wholly owned subsidiary of Lockheed Martin Corporation, for the U.S. Department of Energys National Nuclear Security Administration under contract DE-AC04-94AL85000.

The development of the exponentially fitted Scharfetter-Gummel (SG) scheme [25] was a major breakthrough that enabled stable and accurate numerical solution of the drift-diffusion equations in one-dimension. Extension of SG to multiple dimensions [16, 12, 26] typically relies on topologically dual grids<sup>†</sup>; see the right plot in Fig. 1. For such grids, the area of the dual (control volume) side times the SG edge current on the primal edge crossing that side gives an accurate approximation of the current density flux through the boundary of the dual cell. The resulting SG-BIM (Box Integration Method, or Finite Boxes approach) scheme has excellent stability and is the workhorse in most modern device simulators [9, 15, 12].

Insofar as conservation of current density is concerned, finite volume and finite element methods follow different paths. The former integrate the continuity equation on the (topologically dual) control volumes and apply the Divergence Theorem to transform the volume integrals into surface integrals. This ensures conservation of current density with respect to the dual control volumes. On the other hand, conservative finite elements approximate the current density by div-conforming *face elements* [6]. The resulting mixed finite element methods [5] have indefinite systems with more variables than primal Galerkin methods, which approximate only the charge density. However, primal Galerkin methods do not conserve current density and so, they lack one of the two desirable properties for device simulations.

The Control Volume Finite Element Method (CVFEM) [3] is an alternative approach that combines the simplicity of the primal Galerkin method with the local conservation properties of finite volume methods, *without requiring topologically dual grids*. The CVFEM approximates charge densities using the same nodal shape functions as the primal Galerkin method. However, the “weak” CVFEM equations result from application of the Divergence Theorem to control volumes surrounding the element vertices, i.e., they resemble finite volume equations.

While the CVFEM is conservative, it still needs some form of stabilization for advection-dominated problems [20, 28, 29]. In this paper we present a new CVFEM for the drift-diffusion equations, which uses exponentially fitted  $H(\text{curl})$ -conforming currents (CVFEM-EFC) to merge the exceptional stability of the SG-BIM with the greater flexibility of CVFEM. In a nutshell, we solve one-dimensional drift-diffusion equations on the edges of the finite element mesh and then use  $H(\text{curl})$ -conforming edge elements [23] to expand the resulting edge current densities into an elemental current density. In so doing we obtain a method that is essentially equivalent to SG-BIM on topologically dual grids, yet remains robust and accurate in the absence of this property, because the elemental current field can be integrated accurately on arbitrary surfaces inside the elements. Computational studies on non-uniform grids using a suite of standard test problems and a more realistic n-channel metal-oxide semiconductor field-effect transistor (MOSFET) device confirm this.

To motivate our approach we examine the nodal CVFEM currents in the pure diffusion limit. Using the fact that nodal and edge elements are part of an exact sequence we prove that in the absence of carrier drift the nodal current is sum of edge currents from one-dimensional diffusion problems times  $H(\text{curl})$ -conforming edge basis functions. Therefore, the exponentially fitted  $H(\text{curl})$ -conforming current in this paper represents a consistent extension of the nodal current density.

The use of  $H(\text{curl})$ -conforming elements to extend edge currents into an elemental current density, and independence from explicit stabilization parameters differentiate the CVFEM-EFC from other stabilized CVFEM formulations [29, 28]. These papers stabilize the CVFEM using the same perturbation functions as the SUPG method [8]. The resulting CVFEMs inherit the SUPG stabilization parameter and the quality of their solutions depends critically on the choice of this parameter. Finding the optimal stabilization parameter for a given PDE configuration remains an

<sup>†</sup>We remind the reader that two grids in  $d$ -dimensions are topologically dual if there is one-to-one correspondence between their  $k$  and  $d - k$ -dimensional entities. For example, in three dimensions ( $d = 3$ ) every primal vertex ( $k = 0$ ) corresponds to a unique dual cell ( $3 - 0 = 3$ ); every primal edge ( $k = 1$ ) corresponds to a unique dual face ( $3 - 1 = 2$ ), every primal face ( $k = 2$ ) corresponds to a unique dual edge ( $3 - 2 = 1$ ), and every primal cell ( $k = 3$ ) corresponds to a unique dual vertex ( $3 - 3 = 0$ ). In two dimensions ( $d = 2$ ) the correspondence is between primal vertices ( $k = 0$ ) and dual cells ( $2 - 0 = 2$ ), primal sides ( $k = 1$ ) and dual sides ( $2 - 1 = 1$ ) and primal cells ( $k = 2$ ) and dual vertices ( $2 - 2 = 0$ ).

open problem. Some of the parameters that enter its definition are not known exactly [13], and different solution features, such as internal discontinuities and boundary layers, require different definitions of this parameter [14].

Our brief survey deliberately omits approaches which use the primal Galerkin formulation of the drift-diffusion equations because it lacks the second desirable property, i.e., the local current conservation. We refer the interested readers to [27] (extension of SUPG to drift-diffusion), [1, 24, 32, 31] (exponentially fitted conforming finite elements), and [30] (stabilized Generalized Finite Element) for examples and further details. Likewise, we skip mixed methods for drift-diffusion because of their more complicated computational structure, which does not allow simple reuse of an existing primal Galerkin code infrastructure. We refer to [6, 7] for more information about these methods.

The rest of this section reviews the relevant notation and the model drift-diffusion equations. The core of this paper is Section 2 where we motivate and define the CVFEM-EFC formulation. Section 3 briefly discusses implementation of the method and Section 4 uses Cartesian grids to shed some light on the distinctions between CVFEM-EFC and SG-BIM. Section 5 presents numerical results and Section 6 summarizes our conclusions.

### 1.1. Notation

In this paper  $\Omega$  is a bounded region in  $\mathbb{R}^n$ ,  $n = 2, 3$  with Lipschitz-continuous boundary  $\partial\Omega$ . The Neumann and Dirichlet parts of the boundary are  $\Gamma_N$  and  $\Gamma_D$ , respectively. We use the standard notation  $H^1(\Omega)$  for the Sobolev space of order one,  $L^2(\Omega)$  for the space of all square integrable functions, and  $H(\text{curl}, \Omega)$  for the space of all square integrable vector fields whose curl is also square integrable. Lower case Roman and Greek letters denote scalar quantities and bold face symbols are vector quantities. The meaning of the symbol  $|\cdot|$  varies with the context and can be Euclidean length, domain measure, or cardinality of a finite set.

Throughout the paper  $K_h(\Omega)$  is a conforming finite element partition of  $\Omega$  into elements  $K_s$  with size  $h_s$  and barycenter  $\mathbf{b}_s$ . The average element size in  $K_h(\Omega)$  is  $h > 0$ . The vertices of the mesh are  $\mathbf{v}_i$  and  $\mathbf{e}_{ij}$  is a mesh edge with endpoints  $\mathbf{v}_i$  and  $\mathbf{v}_j$ . The midpoint and the length of  $\mathbf{e}_{ij}$  are

$$\mathbf{m}_{ij} = \frac{\mathbf{v}_i + \mathbf{v}_j}{2} \quad \text{and} \quad h_{ij} = |\mathbf{v}_i - \mathbf{v}_j|,$$

respectively. The vertices, edges, sides, and elements intersecting with entity  $\Xi$  are  $V(\Xi)$ ,  $E(\Xi)$ ,  $S(\Xi)$ , and  $K(\Xi)$ , respectively. For example,  $V(\Omega)$  is the set of all mesh vertices,  $E(\Omega)$  is the set of all mesh edges,  $V(K_s)$  are the vertices of element  $K_s$ ,  $E(\mathbf{v}_i)$  are all edges having  $\mathbf{v}_i$  as a vertex,  $K(\mathbf{e}_{ij})$  are the elements sharing  $\mathbf{e}_{ij}$ , and so on. Note that in two-dimensions  $E(\Xi) = S(\Xi)$ . Selection of vertex ordering induces orientation of  $\mathbf{e}_{ij} \in E(\Omega)$ :

$$\sigma_{ij} = \begin{cases} -1 & \text{if } \mathbf{v}_i \text{ is the first vertex of } \mathbf{e}_{ij}, \text{ i.e., the vertex order is } \mathbf{v}_i \rightarrow \mathbf{v}_j \\ 1 & \text{if } \mathbf{v}_i \text{ is the second vertex of } \mathbf{e}_{ij}, \text{ i.e., the vertex order is } \mathbf{v}_i \leftarrow \mathbf{v}_j \end{cases} \quad (1)$$

The unit tangent on  $\mathbf{e}_{ij}$  follows the edge orientation

$$\mathbf{t}_{ij} = \sigma_{ij} \frac{\mathbf{v}_i - \mathbf{v}_j}{|\mathbf{v}_i - \mathbf{v}_j|},$$

and always points towards the *second* vertex of the edge.

We refer to Fig. 1 for a representative control volume  $C_i$  associated with vertex  $\mathbf{v}_i$  on an unstructured grid. The set of all control volumes forms a dual grid  $K'_h(\Omega)$  with dual vertices  $V'$ , dual edges  $E'(\Omega)$ , and dual sides  $S'(\Omega)$ . Every primal edge  $\mathbf{e}_{ij}$  corresponds to a dual control volume side  $\partial C_{ij}$ , which is comprised of *facets*  $\partial C_{ij}^s = \partial C_{ij} \cap K_s, \forall K_s \in K(\mathbf{e}_{ij})$  that is,

$$\partial C_{ij} = \bigcup_{K_s \in K(\mathbf{e}_{ij})} \partial C_{ij}^s.$$

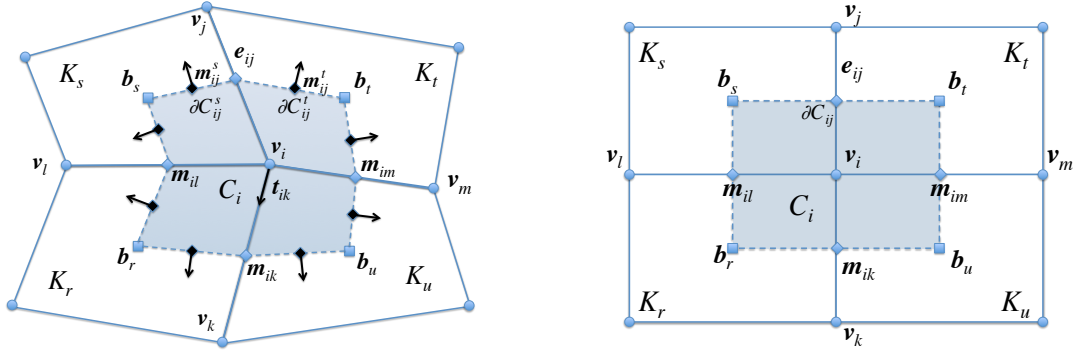


Figure 1. On quadrilateral grids we connect the barycenter  $b_r$  of every  $K_r \in K(v_i)$  with the centers  $m_{ik}$ ,  $m_{il}$  of its two sides connected to  $v_i$ . The resulting control volume  $C_i$  is an octagon. The two sides  $\partial C_{ij}^s$  and  $\partial C_{ij}^t$  of this octagon, which connect to  $m_{ij}$ , are the *facets* of the control volume side  $\partial C_{ij}$  dual to edge  $e_{ij}$ :  $\partial C_{ij} = \partial C_{ij}^s \cup \partial C_{ij}^t$ . On Cartesian grids (right plot) the control volumes  $C_i$  form a topologically dual grid and the unit normals to  $\partial C_{ij}^s$  and  $\partial C_{ij}^t$  are parallel to  $e_{ij}$ . On nonuniform grids (left plot) these normals are not parallel to  $e_{ij}$  and  $C_i$  are not topologically dual to the elements on the primal mesh.

For example, in two-dimensions  $K(e_{ij})$  has two elements and each dual side has two facets:

$$\partial C_{ij} = \partial C_{ij}^s \cup \partial C_{ij}^t, \quad K_s, K_t \in K(e_{ij}).$$

The number of dual sides  $\partial C_{ij}$  always equals the number of edges in  $E(v_i)$ .

The facet  $\partial C_{ij}^s$  of  $\partial C_{ij}$  has barycenter  $m_{ij}^s$  and  $n_{ij}^s$  is its outer unit normal at  $m_{ij}^s$ . A fundamental property of topologically dual grids is that

$$n_{ij}^s = n_{ij}^t = n_{ij} = \pm t_{ij} \quad \forall K_s, K_t \in K(e_{ij}). \quad (2)$$

In other words, the primal edge  $e_{ij}$  is perpendicular to all facets of its dual side  $\partial C_{ij}$ .

Suppose  $C_i$  corresponds to a vertex on the Neumann boundary, i.e.,  $v_i \in \Gamma_N$ . Then

$$\partial C_i = \partial \dot{C}_i \cup \partial C_i^N; \quad \partial \dot{C}_i = \partial C_i \cap \dot{\Omega} \quad \text{and} \quad \partial C_i^N = \partial C_i \cap \Gamma_N. \quad (3)$$

The CVFEM-EFC uses the lowest-order  $H^1(\Omega)$ -conforming and  $H(\text{curl}, \Omega)$ -conforming finite element spaces. In what follows,  $\mathbf{G}^h(\Omega)$  is the  $C^0$  piecewise linear, bilinear or trilinear finite element space and  $\mathbf{C}^h(\Omega)$  is the lowest-order Nedelec edge element space [22]. The latter contains piecewise polynomial vector fields whose tangential component is continuous along the element edges, thus the monicker “edge elements”. The basis of  $\mathbf{G}^h(\Omega)$  is  $\{N_i\}$ ,  $v_i \in V(\Omega)$ . We assume that  $N_i$  is the standard nodal, or Lagrangian basis:

$$N_i(v_j) = \delta_i^j.$$

The basis of  $\mathbf{C}^h(\Omega)$  is  $\{\vec{W}_{ij}\}$ ,  $e_{ij} \in E(\Omega)$ . Two standard unisolvent sets of degrees of freedom for the lowest-order Nedelec element are the mean of the tangent component of  $\vec{W}_{ij}$  along an edge, and the value of this component at the edge midpoint. In this paper we use the former, that is, basis functions<sup>‡</sup> have the property

$$\int_{e_{rs}} \vec{W}_{ij} \cdot \mathbf{t}_{rs} d\ell = \delta_{ij}^{rs}. \quad (4)$$

With this choice at the edge midpoint

$$\vec{W}_{ij} \cdot \mathbf{t}_{rs} \Big|_{m_{rs}} = \frac{\delta_{ij}^{rs}}{h_{rs}}. \quad (5)$$

<sup>‡</sup>The basis functions corresponding to the two unisolvent sets differ only by a scaling factor.

We note that  $\vec{W}_{ij} \cdot \mathbf{t}_{ij} > 0$ , i.e., orientation of the edge basis function  $\vec{W}_{ij}$  always follows the orientation of the associated edge  $\mathbf{e}_{ij}$ .

When  $\Gamma_D$  is non-empty we also need the subspace  $\mathbf{G}_D^h(\Omega)$  of all functions in  $\mathbf{G}^h(\Omega)$ , which vanish on  $\Gamma_D$ , and the subspace  $\mathbf{C}_D^h(\Omega)$  of all fields in  $\mathbf{C}^h(\Omega)$  whose tangential component vanishes on  $\Gamma_D$ .

### 1.2. The drift-diffusion equations

The nonlinear system of PDEs

$$\nabla \cdot (\lambda^2 \mathbf{E}) - (p - n + C) = 0 \quad \text{and} \quad \mathbf{E} = -\nabla \psi \quad \text{in } \Omega \quad (6)$$

$$\frac{\partial n}{\partial t} - \nabla \cdot \mathbf{J}_n + R(\psi, n, p) = 0 \quad \text{and} \quad \mathbf{J}_n = (\mu_n \mathbf{E})n + D_n \nabla n \quad \text{in } \Omega \quad (7)$$

$$\frac{\partial p}{\partial t} + \nabla \cdot \mathbf{J}_p + R(\psi, n, p) = 0 \quad \text{and} \quad \mathbf{J}_p = (\mu_p \mathbf{E})p - D_p \nabla p \quad \text{in } \Omega \quad (8)$$

models the carrier transport in semiconductor materials in terms of the concentrations  $n$  and  $p$  of the electrons and the holes, respectively [26]. We use the standard notation  $\lambda$ ,  $\psi$ ,  $\mathbf{E}$ ,  $\mathbf{J}_n$ , and  $\mathbf{J}_p$  for the minimal Debye length of the device, electric potential, electric field, and electron and hole current densities, respectively. The functions  $D_n$  and  $D_p$  specify carrier's diffusivity, while  $\mu_n$  and  $\mu_p$  are their mobilities. The system (6)–(8) is augmented with the boundary conditions

$$n = n_D \quad \text{and} \quad p = p_D \quad \text{on } \Gamma_D \quad (9)$$

$$\mathbf{J}_n \cdot \mathbf{n} = 0 \quad \text{and} \quad \mathbf{J}_p \cdot \mathbf{n} = 0 \quad \text{on } \Gamma_N. \quad (10)$$

Equation (6) is a simplified model of the electric field in the device and (7)–(8) are the continuity equations for the electron and hole current densities. The terms  $\mu_n n \mathbf{E}$  and  $\mu_p p \mathbf{E}$  are advective fluxes,  $D_n \nabla n$  and  $D_p \nabla p$  are diffusive fluxes, and  $\mathbf{u}_n = \mu_n \mathbf{E}$  and  $\mathbf{u}_p = \mu_p \mathbf{E}$  are carriers drift velocities. When  $D_n \ll \mathbf{u}_n$  and/or  $D_p \ll \mathbf{u}_p$ , the drift-diffusion equations are advection dominated and their solutions can develop internal and/or boundary layers.

## 2. FORMULATION OF THE CVFEM-EFC

The CVFEM-EFC is a marriage of a base CVFEM formulation with a new edge element extension of one-dimensional exponentially fitted edge current densities into the elements. To present the formulation it suffices to consider a single carrier continuity equation. We choose to work with (7) and treat  $\psi$ ,  $\mathbf{E} = -\nabla \psi$ , and  $p$  as given functions. Thus, we focus on the following boundary value problem for the electron concentration  $n$ :

$$\begin{cases} \frac{\partial n}{\partial t} - \nabla \cdot \mathbf{J}_n + R(\psi, n, p) = 0 & \text{and} \quad \mathbf{J}_n = \mu_n n \mathbf{E} + D_n \nabla n & \text{in } \Omega \\ n = g & \text{on } \Gamma_D & \text{and} \quad \mathbf{J}_n \cdot \mathbf{n} = f & \text{on } \Gamma_N. \end{cases} \quad (11)$$

For the sake of generality we allow inhomogeneous Dirichlet and Neumann conditions.

### 2.1. The base CVFEM formulation

Integration of the first equation in (11) on control volumes  $C_i$  corresponding to vertices in  $\Omega \cup \Gamma_N$  is the first step in the definition of the base CVFEM [3]. The second step transforms the integrals using the Divergence Theorem:

$$\int_{C_i} \frac{\partial n}{\partial t} dV - \int_{\partial \dot{C}_i} \mathbf{J}_n \cdot \mathbf{n} dS = - \int_{C_i} R(\psi, n, p) dV + \int_{\partial C_i^N} f dS; \quad \forall \mathbf{v}_i \in \dot{\Omega} \cup \Gamma_N \quad (12)$$

Approximation of the electron concentration  $n$  by a finite element function<sup>§</sup>  $n_h(\mathbf{x}, t) \in \mathbf{G}_D^h(\Omega)$  is the final third step, which yields the semidiscrete in space CVFEM formulation

$$\int_{C_i} \frac{\partial n_h}{\partial t} dV - \int_{\partial C_i} \mathbf{J}_n(n_h) \cdot \mathbf{n} dS = - \int_{C_i} R(\psi, n_h, p) dV + \int_{\partial C_i^N} f dS; \quad \forall \mathbf{v}_i \in \dot{\Omega} \cup \Gamma_N. \quad (13)$$

Where the vector field

$$\begin{aligned} \mathbf{J}_n(n_h(\mathbf{x}, t)) &= \mu_n n_h(\mathbf{x}, t) \mathbf{E} + D_n \nabla n_h(\mathbf{x}, t) \\ &= \sum_{\mathbf{v}_j \in \dot{\Omega} \cup \Gamma_N} n_j(t) (\mu_n N_j \mathbf{E} + D_n \nabla N_j) = \sum_{\mathbf{v}_j \in \dot{\Omega} \cup \Gamma_N} n_j(t) \mathbf{J}_n(N_j) \end{aligned} \quad (14)$$

is finite element approximation of the electron current density  $\mathbf{J}_n$  and  $\mathbf{J}_n(N_j)$  are nodal current densities. Selection of a time stepping scheme completes the definition of the fully discrete base CVFEM. Because our focus is on the spatial discretization we leave this choice open and work with the semi-discrete equation (13). Using the nodal basis expansion

$$n_h(\mathbf{x}, t) = \sum_{\mathbf{v}_j \in \dot{\Omega} \cup \Gamma_N} n_j(t) N_j(\mathbf{x}) + \sum_{\mathbf{v}_j \in \Gamma_D} g(\mathbf{v}_j, t) N_j(\mathbf{x}) \quad (15)$$

we see that (13) is equivalent to

$$\begin{aligned} \sum_{\mathbf{v}_j \in \dot{\Omega} \cup \Gamma_N} \frac{\partial n_j(t)}{\partial t} \int_{C_i} N_j dV - \sum_{\mathbf{v}_j \in \dot{\Omega} \cup \Gamma_N} n_j(t) \int_{\partial C_i} \mathbf{J}_n(N_j) \cdot \mathbf{n} dS \\ = - \int_{C_i} R(\psi, n_h, p) dV + \int_{\partial C_i^N} f dS + \sum_{\mathbf{v}_j \in \Gamma_D} g(\mathbf{v}_j, t) \int_{\partial C_i} \mathbf{J}_n(N_j) \cdot \mathbf{n} dS. \end{aligned} \quad (16)$$

When (11) is advection-dominated the base CVFEM can develop the same spurious oscillations that plague primal Galerkin methods for (11). The root cause for this behavior is the inability of the nodal finite element current density (14) to represent accurately the carrier transport between neighboring nodes when the mesh does not resolve solution features such as boundary and/or internal layers. Stabilization of the base CVFEM is an effective alternative to mesh refinement, which may be prohibitively expensive when  $D_n \ll \mu_n \mathbf{E}$ .

## 2.2. The Scharfetter-Gummel procedure

To stabilize the base CVFEM (12) we propose to replace the nodal current density  $\mathbf{J}_n(N_j)$  by an exponentially fitted current density  $\mathbf{J}_E$ , which models more accurately the solution behavior of (11) when  $D_n \ll \mu_n \mathbf{E}$ .

The classical SG procedure computes exponentially fitted estimates of  $\mathbf{J}_n$  along the *primal mesh edges* and is the starting point for the definition of  $\mathbf{J}_E$ . Extension of SG to multiple dimensions in SG-BIM formulations critically depends on property (2) of topologically dual grids, i.e., the fact that the primal edges are perpendicular to the dual sides. In contrast, we extend one-dimensional edge current densities to an elemental current density  $\mathbf{J}_E$  using  $H(\text{curl})$ -conforming elements, thereby rendering this condition unnecessary. To explicate the distinctions between our approach and methods that require topologically dual  $K_h(\Omega)$  and  $K'_h(\Omega)$ , we review a representative SG-BIM formulation on rectangular grids<sup>¶</sup> for which  $K'_h(\Omega)$  is also rectangular. The right plot in Fig. 1 shows a typical patch of rectangular elements and its dual control volume.

<sup>§</sup>Note that  $n_h(\mathbf{x}, t)$  is the same as in a primal Galerkin method.

<sup>¶</sup>Voronoi-Delaunay grids provide an alternative setting for SG-BIM in two-dimensions. The dual Voronoi cells are hexagons whose sides are perpendicular to the sides of the primal triangles.



Formulation of the SG-BIM relies on the same “weak” equations (12) as the base CVFEM, but uses different approximations for the electron concentration and current density. The former is represented by a constant  $n_i$  on each dual cell  $C_i$  and the latter - by a constant  $J_{ij}$  on each dual side  $\partial C_{ij}$ . It is convenient to think of  $n_i$  as an approximation of  $n(\mathbf{x}, t)$  at vertex  $\mathbf{v}_i$ . Likewise,  $J_{ij}$  approximates the outgoing current  $\mathbf{J}_n \cdot \mathbf{n}_{ij}$  at the center  $\mathbf{m}_{ij}$  of  $\partial C_{ij}$ . Application of the midpoint rule to the volume and surface integrals in (12) yields the semi-discrete in space SG-BIM equations

$$\begin{aligned} \frac{\partial n_i(t)}{\partial t} |C_i| - \sum_{\partial C_{ij} \in \partial \dot{C}_i} J_{ij} |\partial C_{ij}| &= -R_i |C_i| + \sum_{\partial C_{ij}^N \in \partial C_i^N} f_i |\partial C_{ij}^N| \quad \forall \mathbf{v}_i \in \dot{\Omega} \cup \Gamma_N \\ n_i(t) &= \left( \int_{C_i} g(\mathbf{x}, t) dV \right) / |C_i| \quad \forall \mathbf{v}_i \in \Gamma_D \end{aligned} \quad (17)$$

The special relationship (2) that holds on topologically dual grids is the “trick” that enables straightforward extension of SG to (17). Owing to (2)

$$J_{ij} \approx \mathbf{J}_n \cdot \mathbf{n}_{ij} \Big|_{\mathbf{m}_{ij}} = \pm \mathbf{J}_n \cdot \mathbf{t}_{ij} \Big|_{\mathbf{m}_{ij}}.$$

In other words, on topologically dual grids an approximation of the current density along a primal edge  $e_{ij}$  simultaneously approximates the outgoing current at the center of its corresponding dual side  $\partial C_{ij}$ . The SG procedure estimates the edge current, thereby providing the necessary value for  $J_{ij}$  in (17). To this end, the SG approach solves a simplified, one-dimensional version of the continuity equation (11) on the primal edges. The resulting approximation of the electron concentration along  $e_{ij}$  incorporates key solution features in the advection-dominated regime and yields a better estimate of the outgoing current than, e.g., the nodal current  $\mathbf{J}_n(N_j)$ .

Let  $e_{ij}$  be an arbitrary primal edge. Without loss of generality we may assume that its orientation  $\sigma_{ij} = -1$ , i.e., the order of its vertices is  $\mathbf{v}_i \rightarrow \mathbf{v}_j$ . The natural length parameter is  $0 \leq s \leq h_{ij}$ . Along  $e_{ij}$  we consider the following stationary one-dimensional boundary value problem (BVP)

$$\begin{cases} \frac{dJ_{ij}}{ds} = 0; & J_{ij} = \mu_n E_{ij} n(s) + D_n \frac{dn(s)}{ds} \\ n(0) = n_i \quad \text{and} \quad n(h_{ij}) = n_j \end{cases} \quad (18)$$

where  $E_{ij} = \mathbf{E} \cdot \mathbf{t}_{ij}$  and the electron concentrations at the endpoints of  $e_{ij}$  are the boundary data. To estimate  $J_{ij}$  we make the following simplifying assumptions. First,  $\mu_n$  and  $D_n$  are constants connected through the Einstein relation

$$\mu_n = \frac{D_n}{\beta} \quad \text{where} \quad \beta = \frac{k_B T}{q}, \quad (19)$$

$q$  is the electron charge,  $k_B$  is the Boltzman constant and  $T$  is the absolute temperature. Second, the electric potential  $\psi$  varies linearly along  $e_{ij}$ . Consequently,

$$E_{ij} = -\frac{(\psi_j - \psi_i)}{h_{ij}}; \quad \psi_i = \psi(\mathbf{v}_i); \quad \psi_j = \psi(\mathbf{v}_j).$$

Under these assumptions the exact solution of (18) yields the classical SG formula<sup>||</sup> for the edge current densities:

$$J_{ij} = \frac{a_{ij} D_n}{h_{ij}} \left[ n_j (\coth(a_{ij}) + 1) - n_i (\coth(a_{ij}) - 1) \right] \quad (20)$$

<sup>||</sup> The alternate formula  $J_{ij} = D_n / h_{ij} [n_j B(-2a_{ij}) - n_i B(2a_{ij})]$ , where  $B(x) = x / (\exp(x) - 1)$ , is less reliable than (20) in finite precision arithmetic.

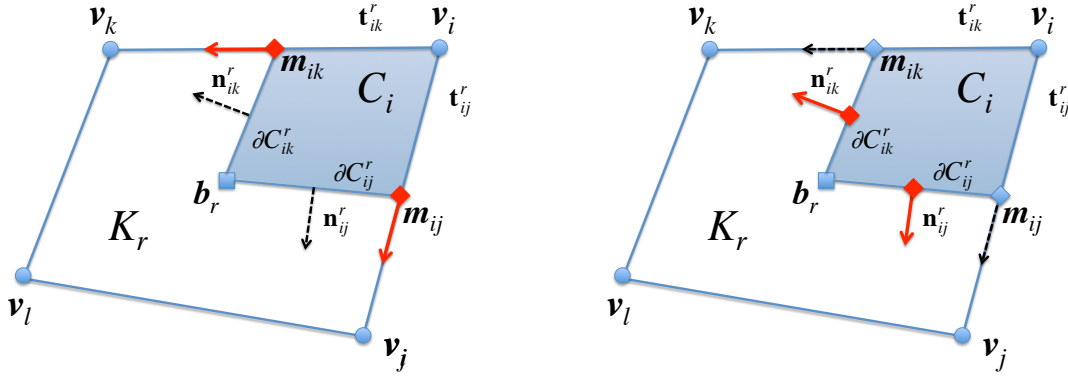


Figure 2. Comparison of the outgoing current density flux approximations by SG-BIM (23) (left pane) and the alternative formula (24) (right pane), when  $K_h(\Omega)$  and  $K_h'(\Omega)$  are not topologically dual. The red diamonds and the red arrows indicate the locations and the directions for the estimates of the outgoing current density, respectively. The SG-BIM continues to use estimates  $J_{ij}$  along the primal edges even though the unit normals on the facets are not parallel anymore to these edges.

where

$$a_{ij} = -\frac{(\psi_j - \psi_i)}{2\beta} = \frac{h_{ij}E_{ij}}{2\beta} \quad (21)$$

is the edge Reynolds number. In summary, (20) produces the following estimate of the outgoing flux through a control volume boundary:

$$\int_{\partial\dot{C}_i} \mathbf{J} \cdot \mathbf{n} dS \approx \sum_{\partial C_{ij} \in \partial\dot{C}_i} \frac{a_{ij} D_n}{h_{ij}} \left[ n_j (\coth(a_{ij}) + 1) - n_i (\coth(a_{ij}) - 1) \right] |\partial C_{ij}| \quad (22)$$

Inserting (22) into (17) completes the definition of SG-BIM.

### 2.3. Exponentially fitted edge element current density

When  $K_h(\Omega)$  and  $K_h'(\Omega)$  are not topologically dual the SG-BIM formulation is prone to significant losses of accuracy. Examples in Section 5.1 demonstrate these losses. To explain the root cause for the diminished accuracy of (17) on unstructured grids we write the approximate surface integrals in SG-BIM as a sum over the dual side's facets:

$$\int_{\partial\dot{C}_i} \mathbf{J} \cdot \mathbf{n} dS \approx \sum_{\partial C_{ij} \in \partial\dot{C}_i} J_{ij} |\partial C_{ij}| = \sum_{\partial C_{ij} \in \partial\dot{C}_i} \sum_{\partial C_{ij}^s \in \partial C_{ij}} J_{ij} |\partial C_{ij}^s|. \quad (23)$$

Because (2) holds only for topologically dual grids, the unit normals to the facets  $\partial C_{ij}^s$  are not parallel to the primal edge  $e_{ij}$ . Consequently, if  $K_h(\Omega)$  is highly unstructured, the edge current density  $J_{ij}$  is a poor estimate of  $\mathbf{J}_n \cdot \mathbf{n}_{ij}^s$  at the center  $\mathbf{m}_{ij}^s$  of facet  $\partial C_{ij}^s$ ; see Fig. 2. Therefore, accurate approximation of the integral on  $\partial C_i$  must account for the distinct normal directions on each facet, as shown on the right in Fig. 2. For example, a better alternative to (23) is the formula

$$\int_{\partial\dot{C}_i} \mathbf{J} \cdot \mathbf{n} dS = \sum_{\partial C_{ij} \in \partial\dot{C}_i} \sum_{\partial C_{ij}^s \in \partial C_{ij}} \int_{\partial C_{ij}^s} \mathbf{J}_n \cdot \mathbf{n} dS \approx \sum_{\partial C_{ij} \in \partial\dot{C}_i} \sum_{\partial C_{ij}^s \in \partial C_{ij}} J_{ij}^s |\partial C_{ij}^s| \quad (24)$$

where  $J_{ij}^s$  approximates  $\mathbf{J}_n \cdot \mathbf{n}_{ij}^s$  at  $\mathbf{m}_{ij}^s$ .

Implementation of integration rules such as (24) depends on the availability of accurate estimates of the current density inside the elements. Calculation of generation rates of electrons  $G_n = \alpha \mathbf{J}_n$  due to impact ionization [16] and generalized mobility models [17] are two other examples that require current density inside the elements. However, the weighted average elemental estimates of  $\mathbf{J}_n$  from SG edge currents in [16, 17] target exclusively SG-BIM schemes on Voronoi-Delaunay grids. As a



result, consistent extension of these estimates to general unstructured grids may be problematic and has not been considered.

Our approach relies on  $H(\text{curl})$ -conforming (edge) finite elements to expand edge currents (20) into an exponentially fitted elemental current density  $\mathbf{J}_E \in \mathbf{C}_D^h(\Omega)$ . Because edge element shape functions are available for a wide range of cell shapes, including polygons [11], this strategy is applicable to an equally wide range of unstructured grids  $K_h(\Omega)$  without requiring that the associated control volume grid  $K'_h(\Omega)$  is topologically dual.

To motivate the use of edge elements we examine the base CVFEM (13) in the absence of carrier drift and establish a relationship between the nodal current  $\mathbf{J}_n(n_h)$  and the edge currents (20).

*Theorem 1*

Assume that carrier drift velocity  $\mu_n \mathbf{E} = 0$ . Then

$$\mathbf{J}_n(n_h) = \sum_{e_{ij} \in E(\Omega)} D_n(n_j - n_i) \vec{W}_{ij}. \quad (25)$$

**Proof.** When  $\mu_n \mathbf{E} = 0$  the nodal current density (14) reduces to

$$\mathbf{J}_n(n_h) = D_n \nabla n_h = \sum_{v_i \in V(\Omega)} D_n n_i \nabla N_i.$$

On the other hand, the nodal space  $\mathbf{G}_D^h(\Omega)$  and the edge element space  $\mathbf{C}_D^h(\Omega)$  belong to an exact sequence (finite element DeRham complex) [2] and so,  $\nabla N_i \in \mathbf{C}_D^h(\Omega)$ . Moreover, in the lowest-order case there holds [4]

$$\nabla N_i = \sum_{e_{ij} \in E(v_i)} \sigma_{ij} \vec{W}_{ij}. \quad (26)$$

Combining these two identities yields the representation

$$\mathbf{J}_n(n_h) = \sum_{v_i \in V(\Omega)} D_n n_i \left( \sum_{e_{ij} \in E(v_i)} \sigma_{ij} \vec{W}_{ij} \right).$$

Without loss of generality we may assume that  $\sigma_{ij} = -1$ , i.e., that the vertex order on  $e_{ij}$  is  $v_i \rightarrow v_j$ . Then, after reordering the terms in the above formula

$$\mathbf{J}_n(n_h) = \sum_{e_{ij} \in E(\Omega)} D_n(n_j - n_i) \vec{W}_{ij}. \quad (27)$$

This concludes the proof.  $\square$

*Corollary 1*

Assume that  $D_n$  is constant along the edges. Under the hypothesis of Theorem 1

$$\mathbf{J}_n(n_h) = \sum_{e_{ij} \in E(\Omega)} h_{ij} J_{ij}^0 \vec{W}_{ij}, \quad (28)$$

where  $J_{ij}^0$  is the solution of (18) in the absence of carrier drift.

**Proof.** In the absence of carrier drift  $\mu_n E_{ij} = 0$  and equation (18) reduces to

$$\begin{cases} \frac{dJ_{ij}^0}{ds} = 0; & J_{ij}^0 = D_n \frac{dn(s)}{ds} \\ n(0) = n_i & \text{and} \quad n(h_{ij}) = n_j. \end{cases} \quad (29)$$

A straightforward calculation shows that

$$n(s) = n_i + s \frac{n_j - n_i}{h_{ij}} \quad \text{and} \quad J_{ij}^0 = D_n \frac{n_j - n_i}{h_{ij}}.$$

Therefore,  $h_{ij}J_{ij}^0 = D_n(n_j - n_i)$ , which completes the proof.  $\square$

The edge current densities  $J_{ij}^0$  are the Scharfetter-Gummel estimates of  $\mathbf{J}_n$  in the absence of carrier drift. Corollary 1 establishes that in the pure diffusion limit the nodal current density is sum of the edge element basis functions times these estimates. This relationship is the departure point for the consistent extension of the edge currents (20) into an elemental current density  $\mathbf{J}_E \approx \mathbf{J}_n$ . Specifically, in the general drift-diffusion case we set

$$\mathbf{J}_E = \sum_{\mathbf{e}_{ij} \in E(\Omega)} h_{ij} J_{ij} \vec{W}_{ij}, \quad (30)$$

where the SG formula (20) defines the coefficients  $J_{ij}$ . The resulting exponentially fitted current density field

$$\mathbf{J}_E = \sum_{\mathbf{e}_{ij} \in E(\Omega)} a_{ij} D_n \left[ n_j (\coth(a_{ij}) + 1) - n_i (\coth(a_{ij}) - 1) \right] \vec{W}_{ij} \quad (31)$$

belongs to  $H(\text{curl}, \Omega)$  and is defined on any mesh that supports construction of Nedelec edge elements. To complete the definition of CVFEM-EFC we replace the nodal current density in the base CVFEM (13) by  $\mathbf{J}_E$ :

$$\int_{C_i} \frac{\partial n_h}{\partial t} dV - \int_{\partial \dot{C}_i} \mathbf{J}_E \cdot \mathbf{n} dS = - \int_{C_i} R(\psi, n_h, p) dV + \int_{\partial C_i^N} f dS; \quad \forall i \in \dot{\Omega} \cup \Gamma_N. \quad (32)$$

We conclude this section with a formal proof that  $\mathbf{J}_E$  is a consistent extension of the representation (28), which motivates its definition (30).

*Lemma 1*

Assume that  $D_n$  and  $\mu_n$  are constant along the edges,  $\mathbf{E} = -\nabla\psi$ , the electric potential  $\psi$  varies linearly between the nodes,  $\mathbf{u}_n = \mu_n \mathbf{E}$  and (30) defines  $\mathbf{J}_E$ . Then

$$\lim_{\mathbf{u}_n \rightarrow 0} \mathbf{J}_E = \mathbf{J}_n(n_h). \quad (33)$$

**Proof.** If  $\mathbf{u}_n \rightarrow 0$  we must have  $E_{ij} \rightarrow 0$  for all  $\mathbf{e}_{ij}$  and from (21) it follows that  $a_{ij} \rightarrow 0$  as well. It is straightforward to see that

$$\lim_{a_{ij} \rightarrow 0} a_{ij} \coth(a_{ij}) = 1,$$

and so, for every  $\mathbf{e}_{ij}$

$$\lim_{a_{ij} \rightarrow 0} J_{ij} = \lim_{a_{ij} \rightarrow 0} \frac{a_{ij} D_n}{h_{ij}} \left[ n_j (\coth(a_{ij}) + 1) - n_i (\coth(a_{ij}) - 1) \right] = \frac{D_n}{h_{ij}} (n_j - n_i) = J_{ij}^0.$$

This concludes the proof.  $\square$

*Remark 1*

The representation of  $\mathbf{J}_E$  in (30) is an instance of a general approach for defining elemental current fields from lower-dimensional estimates. The idea is to seek an  $H(\text{curl})$ -conforming approximation of the current density

$$\mathbf{J}_n \approx \sum_{\alpha} \tilde{J}_{\alpha} \vec{W}_{\alpha}^r, \quad (34)$$

where  $\{\vec{W}_{\alpha}^r\}$  span an edge element space of order  $r$ , and  $\tilde{J}_{\alpha}$  approximate  $\mathbf{J}_n$  on lower-dimensional entities  $\alpha$  of the element. For the lowest-order Nedelec element  $\vec{W}_{ij}$  the sum (34) specializes to

$$\mathbf{J}_n \approx \sum_{\mathbf{e}_{ij} \in E(\Omega)} \tilde{J}_{ij} \vec{W}_{ij},$$

and the normalization property (5) yields the relation

$$\mathbf{J}_n \cdot \mathbf{t}_{kl} \Big|_{\mathbf{m}_{kl}} \approx \sum_{\mathbf{e}_{ij} \in E(\Omega)} \tilde{J}_{ij} \left( \vec{W}_{ij} \cdot \mathbf{t}_{kl} \right) \Big|_{\mathbf{m}_{kl}} = \frac{\tilde{J}_{kl}}{h_{kl}}.$$

The latter implies

$$\tilde{J}_{kl} \approx h_{kl} (\mathbf{J}_n \cdot \mathbf{t}_{kl}) \Big|_{\mathbf{m}_{kl}}. \quad (35)$$

Thus, the lowest-order edge element formula (34) allows us to construct an elemental current density from one-dimensional estimates of  $\mathbf{J}_n \cdot \mathbf{t}_{ij}$  at edge midpoints. In particular, setting  $\tilde{J}_{kl} = h_{ij} J_{ij}$ , yields the exponentially fitted approximation (30). A forthcoming paper will examine the possibility to obtain higher-order elemental estimates of  $\mathbf{J}_n$  from one-dimensional currents by using (34) with higher-order Nedge elements.

### 3. IMPLEMENTATION

The expanded form of the CVFEM-EFC formulation (32) is

$$\sum_{\mathbf{v}_j \in \Omega \cup \Gamma_N} \frac{\partial n_j(t)}{\partial t} \int_{C_i} N_j dV - \sum_{\mathbf{e}_{kl} \in E(\Omega)} J_{kl} \int_{\partial C_i} \vec{W}_{kl} \cdot \mathbf{n} dS = - \int_{C_i} R(\psi, n_h, p) dV + \int_{\partial C_i^N} f dS. \quad (36)$$

With an appropriate discretization in time (36) is equivalent to a linear system of algebraic equations  $\mathbf{K} \vec{n} = \vec{f}$  for the unknown nodal coefficients  $\vec{n} = \{n_j\}_{j \in \Omega \cup \Gamma_N}$  of the discrete carrier concentration (15). The rows of the global discretization matrix  $\mathbf{K}$  correspond to control volumes  $C_i$  surrounding the vertices  $\mathbf{v}_i$  associated with unknown nodal values  $n_i$ .

In this section we explain computation of the contributions from the control volume boundary integrals in (36) to the discretization matrix  $\mathbf{K}$ . Computation of the integrals on  $C_i$  is straightforward. To this end, it is instructive to rewrite (30) in a “vertex” form by collecting all terms that share the same nodal degree of freedom. For a vertex  $\mathbf{v}_j$  these terms correspond to the edges in  $E(\mathbf{v}_j)$ , providing the following equivalent representation of the exponentially fitted current:

$$\mathbf{J}_E = \sum_{\mathbf{v}_j \in \Omega \cup \Gamma_N} \sum_{\mathbf{e}_{jk} \in E(\mathbf{v}_j)} \sigma_{jk} a_{jk} D_n \left[ n_j (\coth(a_{jk}) + \sigma_{jk}) \right] \vec{W}_{jk}. \quad (37)$$

It is now easy to see that the contribution from the second term in (36) to  $\mathbf{K}_{ij}$  is

$$\mathbf{K}_{ij} \leftarrow \sum_{\mathbf{e}_{jk} \in E(\mathbf{v}_j)} \sigma_{jk} a_{jk} D_n \left[ n_j (\coth(a_{jk}) + \sigma_{jk}) \right] \int_{\partial C_i} \vec{W}_{jk} \cdot \mathbf{n} dS.$$

Typically,  $\mathbf{K}_{ij}$  is assembled from element matrices  $\mathbf{K}_{ij}^r$ . The integrals on the facets of  $\partial C_i$  belonging to an element  $K_r$  are the contributions from the control volume boundary integral to the element matrices  $\mathbf{K}_{ij}^r$ :

$$\mathbf{K}_{ij}^r \leftarrow \sum_{\mathbf{e}_{jk} \in E(\mathbf{v}_j) \cap E(K_r)} \sum_{\partial C_{im}^r \in \partial C_i \cap K_r} \sigma_{jk} a_{jk} D_n \left[ n_j (\coth(a_{jk}) + \sigma_{jk}) \right] \int_{\partial C_{im}^r} \vec{W}_{jk} \cdot \mathbf{n} dS. \quad (38)$$

For example, if the mesh is comprised of quadrilateral elements, the control volumes have two facets inside each element and every vertex is attached to two edges of  $K_r$ ; see Figure 3. In this case the element contribution (38) has four terms. Using the notation in Figure 3 these terms are

$$\mathbf{K}_{ij}^r \leftarrow \begin{cases} \sigma_{jl} a_{jl} D_n \left[ n_j (\coth(a_{jl}) + \sigma_{jl}) \right] \left( \int_{\partial C_{ij}^r} \vec{W}_{jl} \cdot \mathbf{n} dS + \int_{\partial C_{ik}^r} \vec{W}_{jl} \cdot \mathbf{n} dS \right) + \\ \sigma_{ji} a_{ji} D_n \left[ n_j (\coth(a_{ji}) + \sigma_{ji}) \right] \left( \int_{\partial C_{ij}^r} \vec{W}_{ji} \cdot \mathbf{n} dS + \int_{\partial C_{ik}^r} \vec{W}_{ji} \cdot \mathbf{n} dS \right) \end{cases}$$

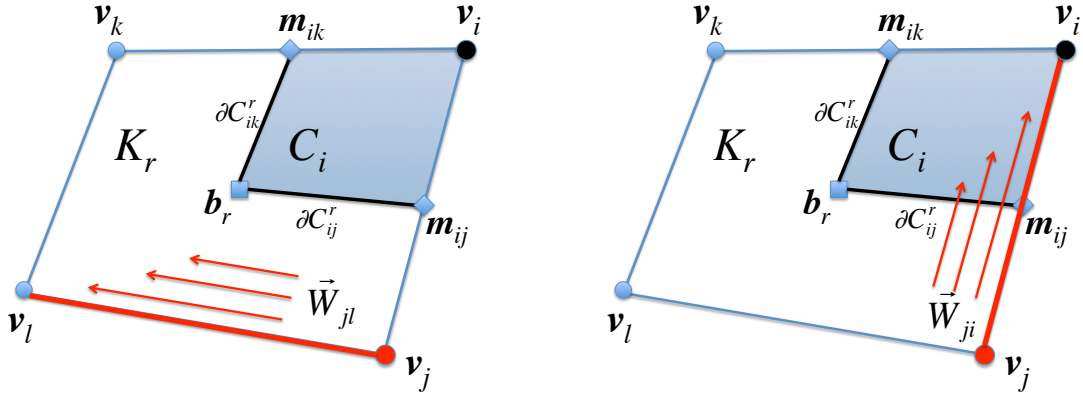


Figure 3. Assembly of the element contribution (38) to  $\mathbf{K}_{ij}^r$  on quadrilateral grids. The control volume  $C_i$  has two facets in  $K_r$ :  $\partial C_i \cap K_r = \partial C_{ik}^r \cup \partial C_{ij}^r$  (black lines). The vertex  $v_j$  corresponding to the unknown  $n_j$  is attached to two edges:  $E(v_j) \cap E(K_r) = \{e_{jl}, e_{ji}\}$  (red lines). As a result, (38) has four different terms corresponding to surface integrals of the two basis functions associated with  $e_{jl}$  and  $e_{ji}$  (the red arrows) on the two control volume facets.

If a nodal coefficient  $n_j$  corresponds to a vertex on the Dirichlet boundary  $\Gamma_D$ , the resulting terms contribute to the right hand side  $\vec{f}$  of the linear system. Finally, we note that practical computation of the element contributions to  $\mathbf{K}$  requires suitable cubature rules for the volume and surface integrals in (36).

#### 4. COMPARISON WITH SG-BIM ON CARTESIAN GRIDS

Comparison of CVFEM-EFC and SG-BIM on uniform Cartesian grid  $K_h(\Omega)$  further clarifies the distinctions between the two methods. Because the dual  $K_h'(\Omega)$  is also uniform Cartesian, it suffices to consider a single control volume  $C_i$ ; see Fig. 4. For simplicity, we assume that all elements in the patch defining the control volume are unit squares and orient their edges to match the outer unit normal on the control volume side to which they contribute currents.

Since all elements are identical we compute their contributions once using the lower right element  $K_r$  with vertices  $v_i, v_j, v_k, v_l$  and edges  $e_{ij}, e_{jk}, e_{lk}, e_{il}$  with orientations  $\sigma_{ij} = \sigma_{jk} = \sigma_{lk} = \sigma_{il} = -1$ . Without loss of generality we place the origin at  $v_j$  so that  $K_r = [0, 1] \times [0, 1]$ . As a result, the edge basis functions for the vertical edges  $e_{lk}$  and  $e_{ij}$  are

$$\vec{W}_{ij} = - \begin{pmatrix} 0 \\ 1 \end{pmatrix} (1-x); \quad \vec{W}_{lk} = - \begin{pmatrix} 0 \\ 1 \end{pmatrix} (x);$$

and the basis functions for the horizontal edges  $e_{jk}$  and  $e_{il}$  are

$$\vec{W}_{jk} = \begin{pmatrix} 1 \\ 0 \end{pmatrix} (1-y); \quad \vec{W}_{il} = \begin{pmatrix} 1 \\ 0 \end{pmatrix} (y).$$

Taking into consideration that the edges of  $K_r$  have unit lengths, (30) specializes to

$$\mathbf{J}_E = \sum_{e_{ij} \in E(K_r)} J_{ij} \vec{W}_{ij} = \begin{pmatrix} 1 \\ 0 \end{pmatrix} [(1-y)J_{jk} + yJ_{il}] - \begin{pmatrix} 0 \\ 1 \end{pmatrix} [(1-x)J_{ij} + xJ_{lk}] \quad (39)$$

Because  $\vec{W}_{jk}$  and  $\vec{W}_{il}$  are parallel to facet  $\partial C_{ij}^r$ , and the midpoint rule is exact for linear functions

$$\int_{\partial C_{ij}^r} \mathbf{J}_E \cdot \mathbf{n} dS = |\partial C_{ij}^r| \left( \mathbf{J}_E \cdot \mathbf{n}_{ij}^r \right) \Big|_{\mathbf{m}_{ij}^r} = \frac{1}{2} [(1-x)J_{ij} + xJ_{lk}] \Big|_{x=0.25} = \frac{3}{8} J_{ij} + \frac{1}{8} J_{lk}$$

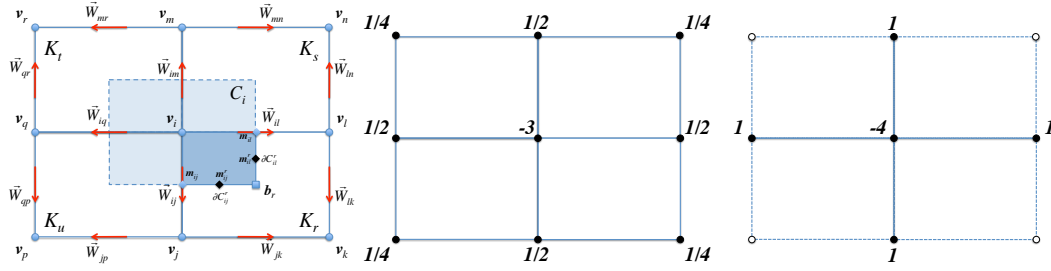


Figure 4. Notation for a patch of square elements and its control volume. Orientation of edge basis functions matches the outer normal direction on the control volume sides. Stencils of CVFEM-EFC and SG-BIM in the pure diffusion limit.

Likewise, because  $\vec{W}_{ij}$  and  $\vec{W}_{lk}$  are parallel to  $\partial C_{il}^r$ ,

$$\int_{\partial C_{il}^r} \mathbf{J}_E \cdot \mathbf{n} dS = |\partial C_{il}^r| \left( \mathbf{J}_E \cdot \mathbf{n}_{il}^r \right) \Big|_{m_{il}^r} = \frac{1}{2} \left[ (1-y)J_{jk} + yJ_{il} \right] \Big|_{y=0.75} = \frac{3}{8}J_{il} + \frac{1}{8}J_{jk}$$

Combining the facet integrals from all elements results in the approximation

$$\int_{\partial C_{ij}} \mathbf{J} \cdot \mathbf{n} dS \approx \frac{1}{8}J_{qp} + \frac{3}{4}J_{ij} + \frac{1}{8}J_{lk} \quad \text{and} \quad \int_{\partial C_{im}} \mathbf{J} \cdot \mathbf{n} dS \approx \frac{1}{8}J_{qr} + \frac{3}{4}J_{im} + \frac{1}{8}J_{ln}$$

for the horizontal sides of the control volume, and

$$\int_{\partial C_{il}} \mathbf{J} \cdot \mathbf{n} dS \approx \frac{1}{8}J_{mn} + \frac{3}{4}J_{il} + \frac{1}{8}J_{jk} \quad \text{and} \quad \int_{\partial C_{iq}} \mathbf{J} \cdot \mathbf{n} dS \approx \frac{1}{8}J_{mr} + \frac{3}{4}J_{iq} + \frac{1}{8}J_{jp}$$

for its vertical sides. In contrast, on the horizontal sides of  $C_i$  the SG-BIM approximation of the outgoing current flux is

$$\int_{\partial C_{ij}} \mathbf{J} \cdot \mathbf{n} dS \approx J_{ij} \quad \text{and} \quad \int_{\partial C_{im}} \mathbf{J} \cdot \mathbf{n} dS \approx J_{im}$$

and on the vertical sides this approximation is

$$\int_{\partial C_{il}} \mathbf{J} \cdot \mathbf{n} dS \approx J_{il} \quad \text{and} \quad \int_{\partial C_{iq}} \mathbf{J} \cdot \mathbf{n} dS \approx J_{iq}.$$

It is worthwhile to compare these formulas in the pure diffusion limit when  $J_{ij} = J_{ij}^0 = D_n(n_j - n_i)$ . It is easy to see that in this case the CVFEM-EFC yields the nine-point stencil for the Laplacian on the left in Fig. 4, whereas SG-BIM generates the classical five point stencil shown on the right in the same figure. In the general case, CVFEM-EFC and SG-BIM correspond to exponentially fitted versions of these stencils.

## 5. NUMERICAL RESULTS

Section 5.1 examines the accuracy and robustness of the CVEM-EFC using a suite of advection test problems on uniform and non-uniform grids. Section 5.2 simulates a metal-oxide semiconductor field-effect transistor (MOSFET) to test the method in a more realistic setting.

### 5.1. Comparative numerical study

The main objective is to demonstrate that the CVFEM-EFC formulation (32) successfully merges the exceptional stability of the classical SG scheme with the generality and the robustness of the

CVFEM. We also want to illustrate and document the severe loss of accuracy in SG-BIM when  $K_h(\Omega)$  and  $K'_h(\Omega)$  are not topologically dual. To this end we use a suite of standard test problems to compare the numerical performance of CVFEM-EFC and SG-BIM on a variety of quadrilateral grids  $K_h(\Omega)$ . The control volume finite element method with streamline upwinding (CVFEM-SU) [29, 28] provides a benchmark for this comparison. The classical SUPG [8] motivates addition of a streamline diffusion term to the nodal current density

$$\mathbf{J}_{SU} = \mathbf{J}_n(n_h) + \tau_h(\mu_n \mathbf{E}) \nabla \cdot ((\mu_n \mathbf{E}) n_h), \quad (40)$$

which defines the CVFEM-SU. The streamline upwind current (40) depends on the stabilization parameter  $\tau_h$ . The paper [29] recommends the value

$$\tau_h|_{K_s} = \left( \coth Pe_s - \frac{1}{Pe_s} \right) \frac{h_s}{2|\mu_n \mathbf{E}|}, \quad Pe_s = \frac{|\mu_n \mathbf{E}| h_s}{2D_n}; \quad \forall K_s \in K_h(\Omega), \quad (41)$$

which we use in our experiments.

**5.1.1. Computational grids** In this section  $\Omega$  is the unit square  $[0, 1] \times [0, 1]$  with boundary  $\Gamma = \Gamma_B \cup \Gamma_T \cup \Gamma_L \cup \Gamma_R$ , where

$$\begin{aligned} \Gamma_B &= \{(x, y) \mid 0 \leq x \leq 1; y = 0\}; & \Gamma_T &= \{(x, y) \mid 0 \leq x \leq 1; y = 1\} \\ \Gamma_L &= \{(x, y) \mid 0 \leq y \leq 1; x = 0\}; & \Gamma_R &= \{(x, y) \mid 0 \leq y \leq 1; x = 1\}. \end{aligned}$$

The grid  $K_h(\Omega)$  is logically rectangular but not necessarily uniform partition of  $\Omega$  into  $N_x \times N_y$  quadrilateral elements. Figure 1 shows the construction of the dual grid  $K'_h(\Omega)$ . Coordinate maps

$$x_{ij} = x(\xi_i, \eta_j, \gamma), \quad y_{ij} = y(\xi_i, \eta_j, \gamma), \quad 0 \leq i \leq N_x, \quad 0 \leq j \leq N_y, \quad (42)$$

where  $\gamma$  is real parameter, and

$$\xi_i = \frac{i}{N_x}, \quad i = 0, \dots, N_x; \quad \text{and} \quad \eta_j = \frac{j}{N_y}, \quad j = 0, \dots, N_y \quad (43)$$

are the initial uniform grid coordinates, specify the positions of the vertices in  $K_h(\Omega)$ . Our study uses four different families of grids.

**Uniform grids.** The coordinate maps  $x(\xi_i, \eta_j, \gamma) = \xi_i$  and  $y(\xi_i, \eta_j, \gamma) = \eta_j$  define a  $N_x \times N_y$  uniform grid  $K_h(\Omega)$ . The control volume grid  $K'_h(\Omega)$  is topologically dual to  $K_h(\Omega)$ .

**Randomly perturbed grids.** Let  $r_x, r_y$  be uniformly distributed random numbers in  $[-1, 1]$ . The coordinate maps

$$x(\xi_i, \eta_j, \gamma) = \xi_i + 0.25h(r_x h^\gamma); \quad y(\xi_i, \eta_j, \gamma) = \eta_j + 0.25h(r_y h^\gamma), \quad \gamma \geq 0 \quad (44)$$

define an  $O(h^\gamma)$  random perturbation of the initial  $N_x \times N_y$  uniform grid. Increasing  $\gamma$  decreases the level of perturbation and makes  $K_h(\Omega)$  and  $K'_h(\Omega)$  closer to being topologically dual. In the tests we use  $\gamma = 0, 1, 2$ . Figure 5 shows the corresponding  $O(1)$ ,  $O(h)$  and  $O(h^2)$  grids.

**Tensor product grids.** The coordinate maps

$$x(\xi, \eta, \gamma) = (1 - \alpha(\gamma))\xi + \alpha(\gamma)\xi^3; \quad y(\xi, \eta, \gamma) = (1 - \alpha(\gamma))\eta + \alpha(\gamma)\eta^2; \quad \alpha(\gamma) = \frac{\sin(4\pi\gamma)}{2}, \quad (45)$$

where  $0 \leq \gamma \leq 1$ , generate a sequence of rectangular, affine tensor-product grids  $K_h(\Omega)$ ; see Fig. 6. The control volume grid  $K'_h(\Omega)$  is topologically dual to  $K_h(\Omega)$ .



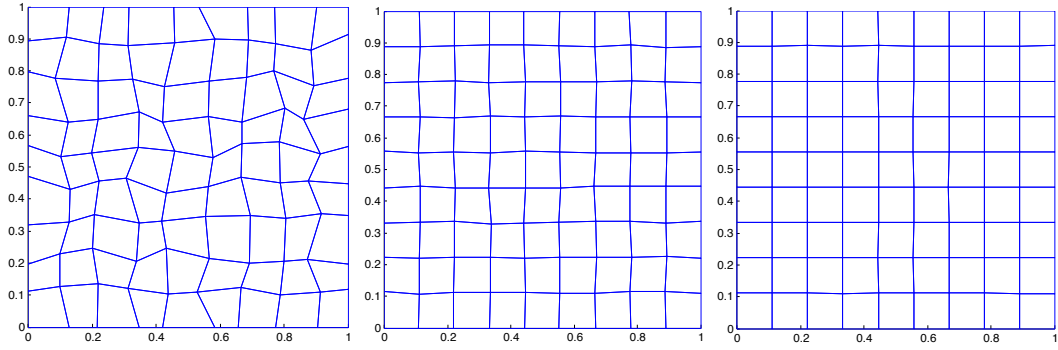


Figure 5. Examples of  $10 \times 10$  randomly perturbed grids. Left pane:  $O(1)$  grid. Center pane:  $O(h)$  grid. Right pane:  $O(h^2)$  grid. The  $O(h^2)$  grid is the closest to the initial uniform grid and its dual  $K'_h(\Omega)$  is the closest to being topologically dual to  $K_h(\Omega)$ . Conversely, the  $O(1)$  grid and its associated control volume grid deviate most from being topologically dual.

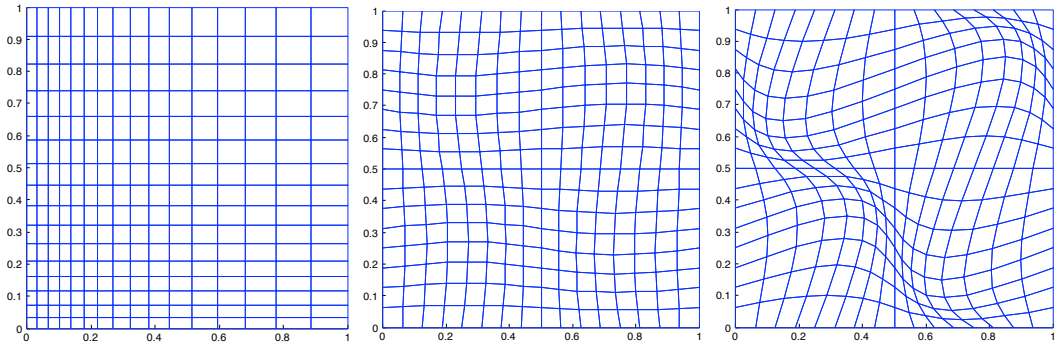


Figure 6. Left pane:  $16 \times 16$  tensor product grid corresponding to (45) with  $\gamma = 0.1$ . Center pane:  $16 \times 16$  smooth grid corresponding to (46) with  $\gamma = 0.1$ . Right pane:  $16 \times 16$  smooth grid corresponding to (46) with  $\gamma = 0.5$ . The tensor product grids have topologically dual control volume grids  $K'_h(\Omega)$ , whereas the smooth grids do not.

**Smooth non-affine grids.** The coordinate maps

$$x(\xi, \eta, \gamma) = \xi + \alpha(\gamma) \sin(2\pi\xi) \sin(2\pi\eta); \quad y(\xi, \eta, \gamma) = \eta + \alpha(\gamma) \sin(2\pi\xi) \sin(2\pi\eta), \quad (46)$$

where  $0 \leq \gamma \leq 1$  and

$$\alpha(\gamma) = \begin{cases} \gamma/5 & \text{if } 0 \leq \gamma \leq 0.5 \\ (1 - \gamma)/5 & \text{if } 0.5 < \gamma \leq 1.0 \end{cases},$$

define non-affine grids  $K_h(\Omega)$  for which the control volume grid  $K'_h(\Omega)$  is not topologically dual to  $K_h(\Omega)$ .

Figure 6 shows examples of tensor product and smooth non-affine grids. We refer to [18] for proof that the maps (45) and (46) generate valid grids for any  $0 \leq \gamma \leq 1$ .

**5.1.2. Test problems** The examples in this section specify steady-state solutions of the governing equations (11). In all examples  $\Gamma_N = \emptyset$ , i.e., we use only Dirichlet boundary conditions. The first two examples are *manufactured solution* problems which prescribe the exact solution  $n(x)$ , the carrier drift velocity  $\mathbf{u}_n = \mu_n \mathbf{E}$ , and the carrier diffusivity  $D_n$ . Substitution of the manufactured solution,  $\mathbf{u}_n$  and  $D_n$  into the governing equation (11) defines the boundary data  $g$  and the recombination term  $R$ . The third example prescribes  $\mathbf{u}_n$ ,  $D_n$ ,  $R$  and the boundary data  $g$ .

**Example 1.** In this problem  $n(x, y) = x^3 - y^2$ , the diffusivity  $D_n = 0.001$ , and the carrier drift velocity  $\mathbf{u}_n = (-\sin \pi/6, \cos \pi/6)$ .

Table I. Comparison of the  $L^2$ -norm and  $H^1$ -seminorm convergence rates of the SG-BIM, CVFEM-EFC and CVFEM-SU methods.

Grid	CVFEM-EFC		SG-BIM		CVFEM-SU	
	$L^2$ error	$H^1$ error	$L^2$ error	$H^1$ error	$L^2$ error	$H^1$ error
32	0.437299E-02	0.762019E-01	0.436418E-02	0.757170E-01	0.576427E-02	0.102676E+00
64	0.210759E-02	0.495408E-01	0.210670E-02	0.493716E-01	0.271216E-02	0.635701E-01
128	0.986937E-03	0.308917E-01	0.986859E-03	0.308385E-01	0.116353E-02	0.351518E-01
Rate	1.095	0.681	1.094	0.679	1.221	0.854

Table II.  $L^2$ -norm and  $H^1$ -seminorm errors in the solution of Example 2 by CVFEM-EFC, SG-BIM and CVFEM-SU on  $64 \times 64$  randomly perturbed, tensor product and smooth nonuniform grids.

Grid type	Error norm	CVFEM-EFC	SG-BIM	CVFEM-SU	Error ratio: EFC/SU
$O(h^2)$	$L^2$	0.8567792E-06	0.7912380E-04	0.1079382E-06	7.93
	$H^1$	0.1440925E-03	0.1317345E-01	0.1629788E-04	8.84
$O(h)$	$L^2$	0.4023762E-04	0.3711650E-02	0.4681861E-05	8.59
	$H^1$	0.6592671E-02	0.6050460E+00	0.7312294E-03	9.01
$O(1)$	$L^2$	0.2085444E-02	0.2272251E+00	0.1974453E-03	10.56
	$H^1$	0.3410112E+00	0.3648320E+02	0.3190555E-01	10.69
Tensor ( $\gamma = 0.1$ )	$L^2$	0.7016708E-02	0.7013024E-02	0.1341020E-03	52.32
	$H^1$	0.1105537E+00	0.1103145E+00	0.3398082E-02	32.53
Smooth ( $\gamma = 0.1$ )	$L^2$	0.5309802E-04	0.8282824E-01	0.1350436E-03	0.39
	$H^1$	0.6165610E-03	0.1414459E+01	0.2479903E-02	0.25
Smooth ( $\gamma = 0.5$ )	$L^2$	0.1264453E-02	0.3789502E+00	0.6498930E-03	1.94
	$H^1$	0.1573398E-01	0.1011258E+02	0.1119514E-01	1.40

**Example 2.** In this problem  $n(x, y) = x + y$  and  $D_n$  and  $\mathbf{u}_n$  are as in Example 1.

**Example 3.** In this problem  $D_n$  and  $\mathbf{u}_n$  are as in Example 1,

$$R = 0 \quad \text{and} \quad g = \begin{cases} 0 & \text{on } \Gamma_L \cup \Gamma_T \cup (\Gamma_B \cap \{x \leq 0.5\}) \\ 1 & \text{on } \Gamma_R \cup (\Gamma_B \cap \{x > 0.5\}) \end{cases}. \quad (47)$$

Discontinuity in the boundary data causes the solution to develop an internal layer of width  $O(\sqrt{D_n})$ , while the homogeneous boundary condition on  $\Gamma_T$  produces an exponential boundary layer. This example specializes [10, Example 3.1.3, p.118] to the unit square.

**5.1.3. Results** The first part of the study compares the asymptotic convergence rates of the CVFEM-EFC, SG-BIM and the benchmark CVFEM-SU. To estimate the rates we solve Example 1 on  $32 \times 32$ ,  $64 \times 64$  and  $128 \times 128$  uniform grids. The results in Table I confirm that all three methods are first-order accurate. The table also shows nearly identical errors and convergence rates for the CVFEM-EFC and SG-BIM. This suggests that on uniform grids the two methods are essentially equivalent. Recall that for such grids the control volume mesh  $K'_h(\Omega)$  is topologically dual to  $K_h(\Omega)$ . We also note that the benchmark CVFEM-SU has slightly higher convergence rates but larger errors.

The second part of the study compares the accuracy of the CVFEM-EFC and SG-BIM on five different non-uniform grids. We use Example 2, which has linear solution. Both CVFEM-EFC and SG-BIM are first-order accurate and won't recover this exact solution. However, linearity makes it easier to visualize the loss of accuracy in SG-BIM on non-topologically dual grids. The CVFEM-SU again provides the benchmark solution.

Table II and Figures 7-8 summarize our results. On the tensor product grid we observe almost identical errors in the CVFEM-EFC and SG-BIM solutions. This reprises the behavior of the two

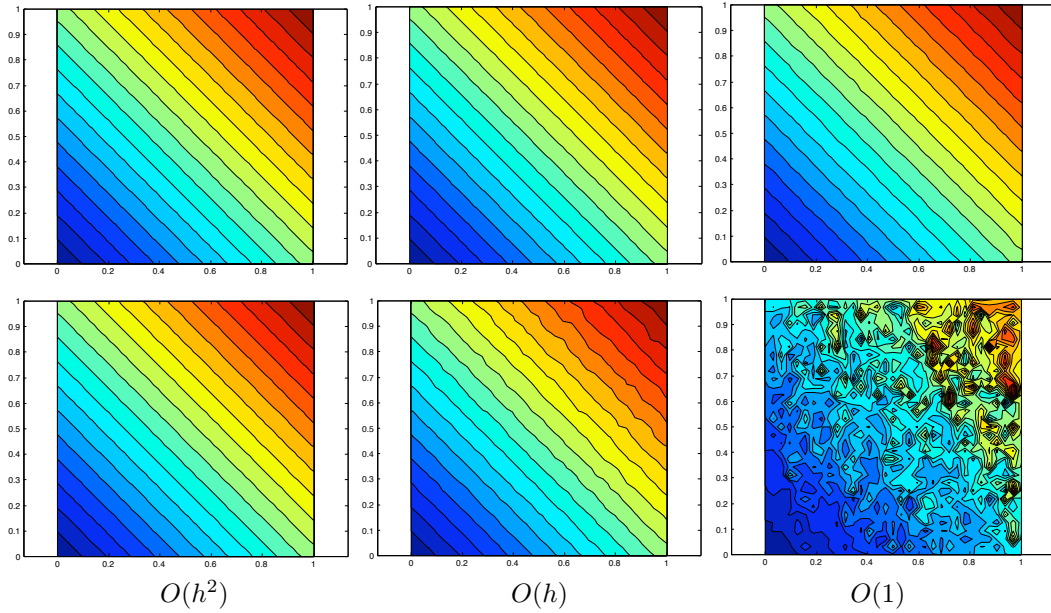


Figure 7. Approximation of a globally linear function by CVFEM-EFC (top row) and SG-BIM (bottom row) on  $64 \times 64$  randomly perturbed grids. Left:  $O(h^2)$  grid. Center:  $O(h)$  grid. Right:  $O(1)$  grid.

methods on uniform grids and is consistent with the fact that, as in the former case, the tensor product grid has a topologically dual control volume grid.

The error ratios in Table II verify that on the randomly perturbed grids the accuracy of CVFEM-EFC roughly matches the accuracy of the benchmark CVFEM-SU. On the  $O(h^2)$  grid, which is close to a uniform grid, the SG-BIM errors are two orders of magnitude greater but the solution is still reasonably accurate. However, as the strength of the perturbation increases to  $O(h)$  and  $O(1)$  the SG-BIM solution deteriorates to a point where the results on the  $O(1)$  grid are unusable; see Fig. 7. The severity of the loss of accuracy in SG-BIM correlates with the severity of the loss of topological duality on the  $O(h^2)$ ,  $O(h)$  and  $O(1)$  grids.

Calculations on smooth non-uniform grids with  $\gamma = 0.1$  and  $\gamma = 0.5$  provide an example of a more subtle loss of accuracy in the SG-BIM. As  $\gamma$  increases from 0.1 to 0.5, the loss of topological duality between  $K_h(\Omega)$  and  $K'_h(\Omega)$  becomes more pronounced and the errors in the SG-BIM solution grow accordingly; see Fig. 8. Yet, unlike the  $O(1)$  random grid case, there are no telltale signs, such as spurious oscillations, to signal the loss of accuracy. Instead, the degradation of the numerical solution manifests itself as a smooth mesh imprinting that is hard to detect without knowledge of the exact solution. The error ratios in Table II again confirm that the CVFEM-EFC solution is roughly of the same accuracy as the benchmark CVFEM-SU solution.

The final part of our study demonstrates some advantages stemming from the absence of tunable stabilization parameters in the CVFEM-EFC. The constant advection test problem (47) provides an appropriate setting for this task because it has both an internal and a boundary layer. The middle plots in Fig. 9 show that the CVFEM-SU with the stabilization parameter (41) has significant overshoots across both layers. However, simply increasing the strength of the stabilization term turns out to be detrimental to the accuracy of the CVFEM-SU. The right plots in Fig. 9 correspond to (41) scaled by a factor of 5 and confirm this. The extra diffusion does not fully eliminate the overshoot across the internal layer, but it smears significantly\*\* the boundary layer. Clearly, the quality of the CVFEM-SU solution depends critically on the choice of the stabilization parameter. Yet, optimal

\*\*A thorough discussion of this subject, including remedies such as discontinuity capturing, is beyond the scope of this paper. We only mention the paper [14], which suggests an alternative definition of the stabilization parameter for elements on the outflow Dirichlet boundary where the boundary layer develops.

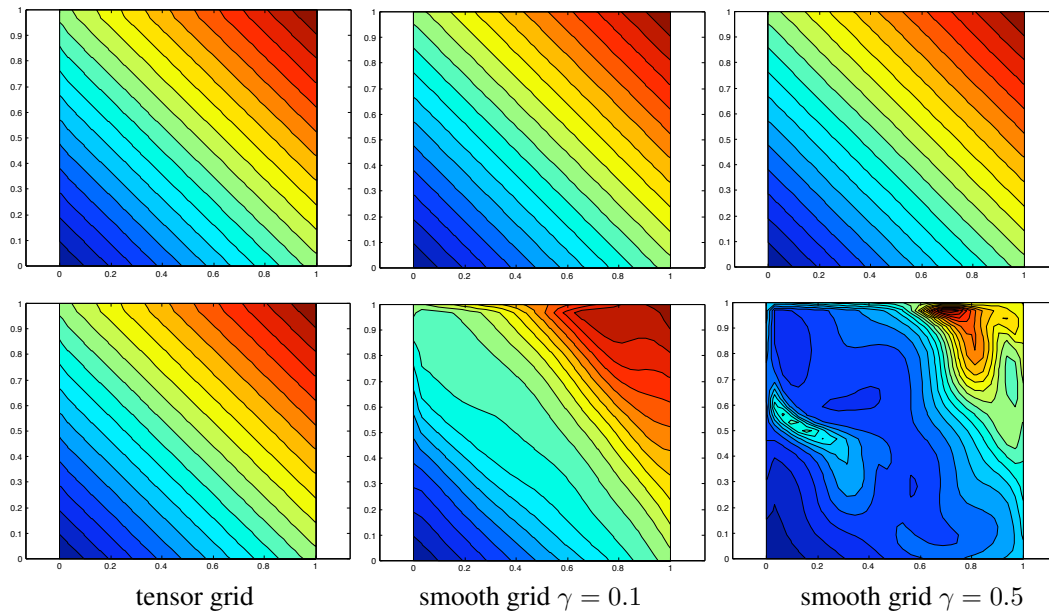


Figure 8. Approximation of a globally linear function by CVFEM-EFC (top row) and SG-BIM (bottom row) on  $64 \times 64$  structured nonuniform grids. Left: tensor product grid. Center: smooth grid with  $\gamma = 0.1$ . Right: smooth grid with  $\gamma = 0.5$ .

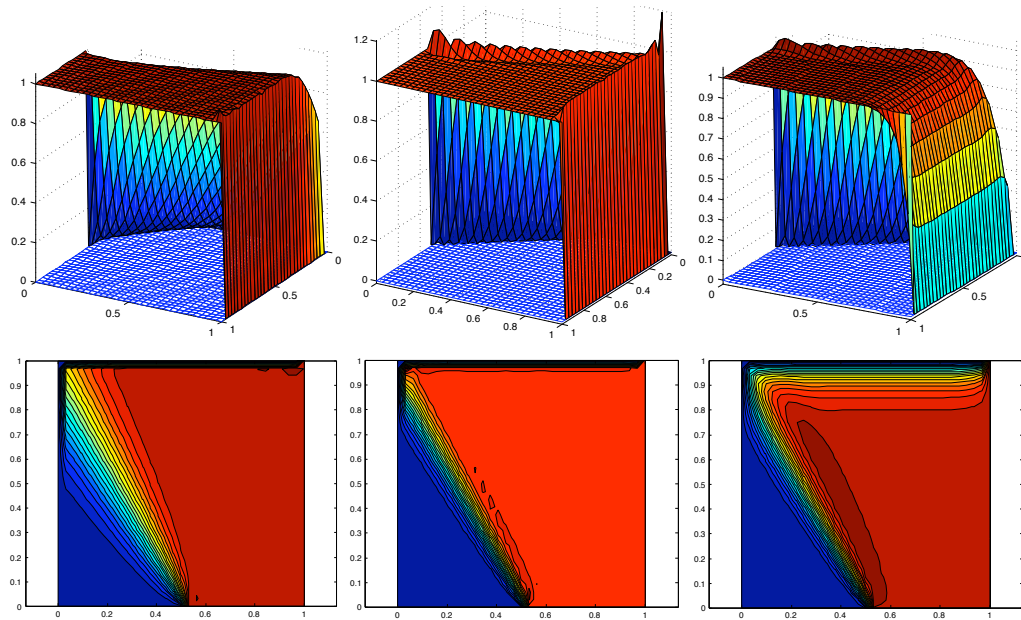


Figure 9. Comparison of CVFEM-EFC and CVFEM-SU solutions of the constant advection test problem (47) on  $33 \times 33$   $O(h)$  grid. Left: the CVFEM-EFC solution. Center: the CVFEM-SU with (41). Right: CVFEM-SU with (41) scaled by 5.

selection of this parameter remains an open problem and can be different for different PDEs. In contrast, the CVFEM-EFC formulation automatically adjusts to the solution features and performs robustly without any additional calibration and/or adaptation to the problem being solved.

### 5.2. MOSFET example

For a more realistic example we consider an n-channel metal-oxide semiconductor field-effect transistor (MOSFET) device shown in Figure 10. A thin silicon dioxide layer ( $\Omega_{ox}$ ) adjacent to the gate electrode and the main silicon body ( $\Omega_{si}$ ) form the MOSFET device structure. Within the body where the source and drain terminals are connected there are highly doped regions with doping concentrations  $N_d$  that differ from the doping concentration of the main body  $N_a$ . For the device modeled here, the silicon dioxide layer has a thickness of 50 nm and a length of 7  $\mu m$ . The total length of the MOSFET device is 8  $\mu m$  and the height of the silicon region is 4  $\mu m$ .

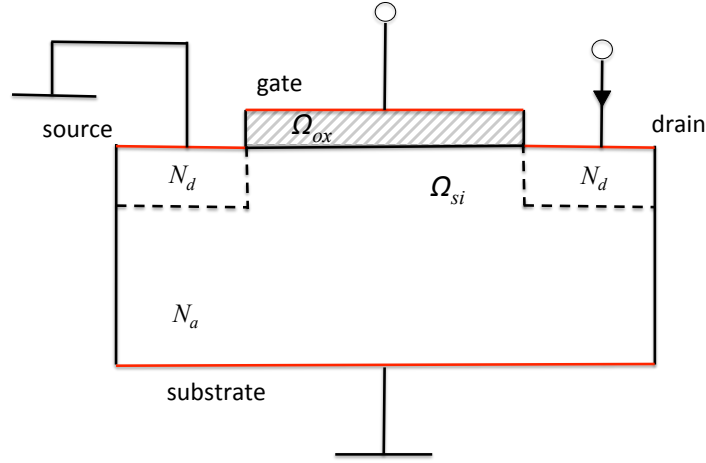


Figure 10. Configuration of an N-channel MOSFET device.

The governing equations for the n-channel MOSFET device consist of a Laplace equation for electric potential ( $\psi$ ) in the silicon dioxide layer, a Poisson equation for the electric potential in the main body, and a continuity equation for the electron concentration ( $n$ ) in the main body:

$$\begin{aligned} \nabla \cdot (\epsilon_0 \epsilon_{ox} \nabla \psi) &= 0 & \text{in } \Omega_{ox} \\ \nabla \cdot (\epsilon_0 \epsilon_{si} \nabla \psi) &= -q \left( n_i \exp\left(\frac{-q\psi}{k_B T}\right) - n + N_d - N_a \right) & \text{in } \Omega_{si} \\ \nabla \cdot (n \mu_n \nabla \psi - D_n \nabla n) &= 0 & \text{in } \Omega_{si} \end{aligned} \quad (48)$$

We refer to Table III for description of the parameters in the MOSFET model.

Parameter	Value	Description
$\epsilon_0$	$8.854 \times 10^{-12} \text{ Fm}^{-1}$	vacuum permittivity
$\epsilon_{si}$	11.9	Silicon dielectric constant
$\epsilon_{ox}$	3.9	Silicon dioxide dielectric constant
$k_B$	$1.380 \times 10^{-23} \text{ J/K}$	Boltzmann constant
$q$	$-1.602 \times 10^{-19} \text{ C}$	electron charge
$T$	300 K	temperature
$\mu_n$	$550 \text{ cm}^2/(\text{Vs})$	electron mobility
$D_n$	$\mu_n k_B T / q$	electron diffusivity
$N_d$	$1.0 \times 10^{17} \text{ cm}^{-3}$	doping concentration in doped regions
$N_a$	$1.0 \times 10^{15} \text{ cm}^{-3}$	doping concentration in main silicon body
$C_0$	$1.0 \times 10^{15} \text{ cm}^{-3}$	scaling parameter for $n$
$\mu_0$	$550 \text{ cm}^2/(\text{Vs})$	scaling parameter for $\mu_n$
$V_0$	$k_B T / q$	scaling parameter for $\psi$
$D_0$	$\mu_0 V_0$	scaling parameter for electron diffusivity
$\tilde{n}_{source}$	100	scaled source boundary value
$\tilde{n}_{drain}$	100	scaled drain boundary value
$\tilde{n}_{substrate}$	$2.1025 \times 10^{-10}$	scaled substrate boundary value

Table III. Summary of parameters for n-channel MOSFET simulation

To test the CVFEM-EFC it is not necessary to solve the coupled system (48). Instead, we use Sandia's device simulation code CHARON to run a fully coupled finite element simulation of the governing equations to generate an approximation  $\psi_h$  of the electric potential in  $\Omega_{si}$ . Figure 11 shows the scaled electric potential from the fully coupled simulation of (48). Treating this

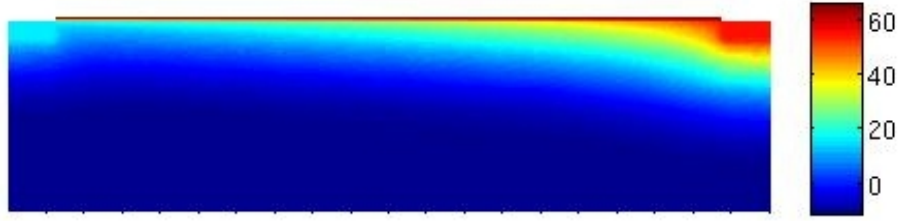


Figure 11. Scaled electric potential used for solution of the electron continuity equation.

potential as an input for the electron continuity equation in the silicon region allows us to separate this equation from the rest of the model, while suitable scaling improves its numerical properties. Specifically, we set the scaled electron density to  $\bar{n} = n/C_0$  for  $C_0 = 1.0 \times 10^{15}$ , the scaled electron mobility is  $\bar{\mu}_n = \mu_n/\mu_0$  for  $\mu_0 = 550$ , the scaled electric potential is  $\bar{\psi}_h = \psi_h/V_0$  for  $V_0 = k_B T/q$ , and the scaled electron diffusivity is  $\bar{D}_n = D_n/D_0$  for  $D_0 = \mu_0 V_0$ . In summary, we apply the CVFEM-EFC to solve the following scaled electron continuity equation

$$\nabla \cdot \bar{\mathbf{J}}_n = 0 \quad \text{and} \quad \bar{\mathbf{J}}_n = \bar{n} \bar{\mu}_n \nabla \bar{\psi}_h - \bar{D}_n \nabla \bar{n} \quad \text{in} \quad \Omega_{si}. \quad (49)$$

where  $\bar{\mu}_n$  and  $\bar{D}_n$  are both equal to one. We impose the following (scaled) Dirichlet boundary conditions for  $\bar{n}$

$$\bar{n}_{source} = N_d/C_0; \quad \bar{n}_{drain} = N_d/C_0; \quad \bar{n}_{substrate} = \frac{n_i^2}{N_a C_0}.$$

At the silicon/silicon dioxide interface and at the boundaries without contacts we impose the Neumann condition  $\bar{\mathbf{J}}_n \cdot \mathbf{n} = 0$ .

The numerical simulation of (49) uses a partition  $K_h(\Omega)$  of the MOSFET device (10) into quadrilateral elements and the parameter values in Table III. The mesh is refined in the doped regions, the silicon dioxide layer, and along the channel region as displayed in Figure 12. The

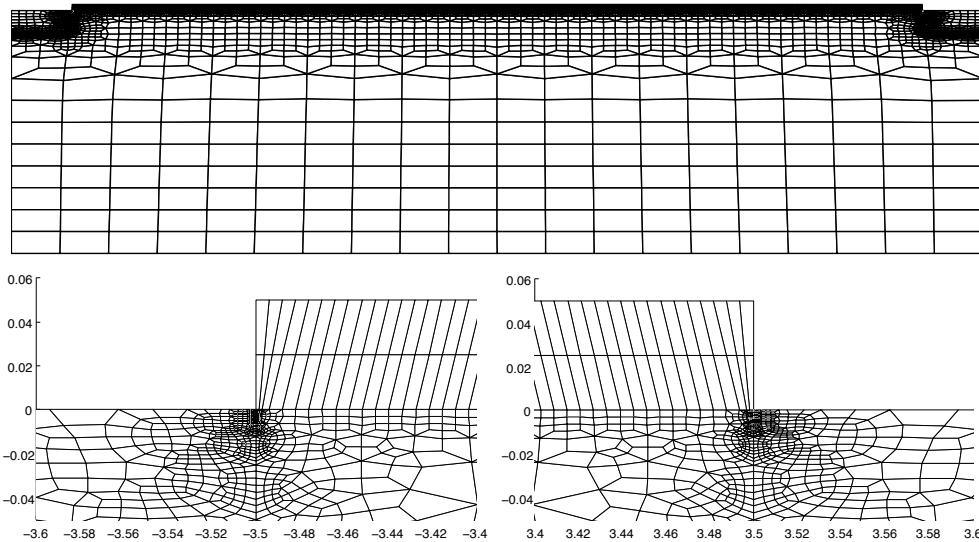


Figure 12. Top row is the unstructured quadrilateral mesh for the n-channel MOSFET device. The bottom row shows the grid refinement in the upper left and the upper right sections of the device.



resulting grid is both highly non-uniform and logically non-rectangular, i.e.,  $E(v_i)$  does not equal 4 in all cases. In particular, Figure 12 shows that in the refined regions  $E(v_i)$  varies between 3 and 6. This represents an additional challenge for methods which rely on topological duality of the control volumes.

To demonstrate this challenge we first solve (49) for the manufactured solution in Example 1. Figure 13 shows that the CVFEM-EFC solution correctly represents the linear function despite the highly unstructured nature of the grid in the upper left and right regions. In contrast, the SG-BIM solution shows significant numerical errors. The strength of these errors correlates with the regions where the grid deviates the most from a logically rectangular topology, i.e., where  $E(v_i) \neq 4$ .

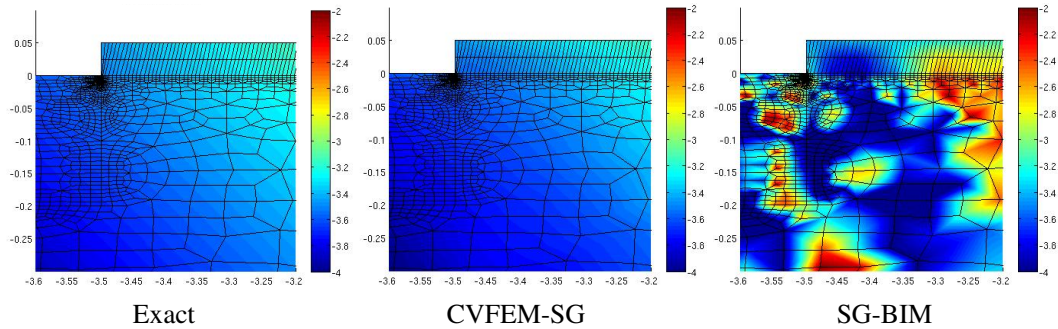


Figure 13. Approximation of a globally linear function on the MOSFET grid. The plots show the exact solution, the CVFEM-EFC solution and the SG-BIM solution in the upper left portion of the device.

Then we proceed to solve (49) using the approximate electric potential  $\psi_h$  in Figure 11 from the fully coupled CHARON solution. Figure 14 shows the scaled electron density for the whole domain resulting from the CVFEM-EFC simulation. The density is highest along the channel that



Figure 14. Scaled electron density for the n-channel MOSFET computed with the CVFEM-EFC shown over the full device.

forms below the silicon dioxide layer and between the two doped regions. Figure 15 provides a more detailed view of the structure of electron density near the source and drain doping regions.

These results agree qualitatively with the fully coupled CHARON solution. They also demonstrate that CVFEM-EFC solution remains stable and is not affected adversely by the lack of a logically rectangular grid structure or the large variations in element sizes in the grid.

## 6. CONCLUSIONS

We presented a new control volume finite element method for the drift-diffusion equations (CVFEM-EFC). The new method combines the exceptional stability of the classical Scharfetter-Gummel upwinding with the generality of CVFEM. On topologically dual grids the CVFEM-EFC is essentially equivalent to the Scharfetter-Gummel Box Integration Method (SG-BIM). However, computational studies in this paper conclusively demonstrate that topological duality of  $K_h(\Omega)$  and  $K'_h(\Omega)$  is *not necessary* for the stability and accuracy of the CVFEM-EFC formulation. The new

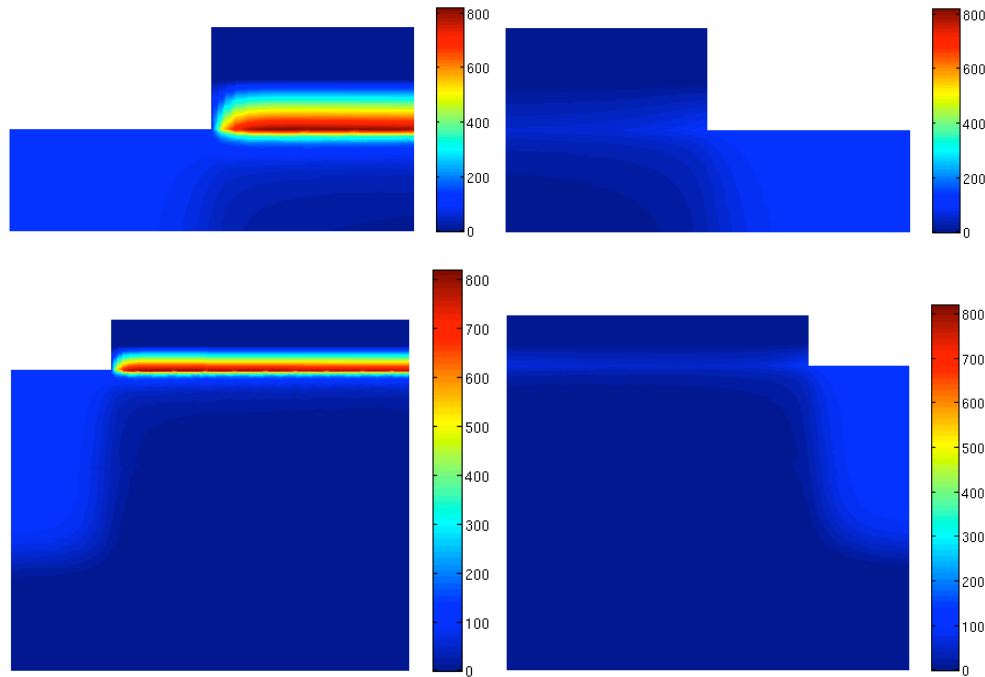


Figure 15. Scaled electron density for the n-channel MOSFET computed with the CVFEM-EFC shown over a small section near the source doping region (left) and the drain doping region (right).

method performs robustly on all grids in the studies. Furthermore, the method adapts automatically to different types of solution features and does not require heuristic stabilization parameters.

On the other hand, our study confirms that topological duality is a *prerequisite* for stable and accurate SG-BIM solution. Without this property (23) fails to provide accurate approximation of the control volume surface integrals. Moreover, violation of topological duality by the control volume mesh  $K'_h(\Omega)$  not only reduces the accuracy but may lead to unphysical solutions and spurious oscillations.

## ACKNOWLEDGMENT

The authors acknowledge funding by the DOE's Office of Science Advanced Scientific Computing Research Program (ASCR). The Advanced Simulation & Computing (ASC) program of the National Nuclear Security Administration (NNSA) supported implementation and testing of the CVFEM-EFC.

Conversations with our colleagues G. Hennigan, L. Musson and T. Smith greatly improved our understanding of device modeling and simulation. J. Aidun lent his support and encouraged us to complete this work despite the many challenges. We owe special thanks to Xujiao Gao for her help with CHARON and especially for generating the electric potentials for the MOSFET simulations in this paper.

## REFERENCES

1. Lutz Angermann and Song Wang. Three-dimensional exponentially fitted conforming tetrahedral finite elements for the semiconductor continuity equations. *Applied Numerical Mathematics*, 46(1):19–43, 2003.
2. D. N. Arnold, R. S. Falk, and R. Winther. Finite element exterior calculus, homological techniques, and applications. *Acta Numerica*, 15:1–155, 2006.
3. B.R. Baliga and S.V Patankar. New finite element formulation for convection-diffusion problems. *Numerical Heat Transfer*, 3(4):393–409, October 1980.

4. P. Bochev and M. Hyman. Principles of mimetic discretizations. In D. N. Arnold, P. Bochev, R. Lehoucq, R. Nicolaides, and M. Shashkov, editors, *Compatible Discretizations, Proceedings of IMA Hot Topics Workshop on Compatible Discretizations*, volume IMA 142, pages 89–120. Springer Verlag, 2006.
5. F. Brezzi and M. Fortin. *Mixed and Hybrid Finite Element Methods*. Springer, Berlin, 1991.
6. Franco Brezzi, Luisa Donatella Marini, and Paola Pietra. Numerical simulation of semiconductor devices. *Computer Methods in Applied Mechanics and Engineering*, 75(1-3):493 – 514, 1989.
7. Franco Brezzi, Luisa Donatella Marini, and Paola Pietra. Two-dimensional exponential fitting and applications to drift-diffusion models. *SIAM Journal on Numerical Analysis*, 26(6):1342–1355, 1989.
8. Alexander N. Brooks and Thomas J.R. Hughes. Streamline upwind/petrov-galerkin formulations for convection dominated flows with particular emphasis on the incompressible navier-stokes equations. *Computer Methods in Applied Mechanics and Engineering*, 32(1&3):199 – 259, 1982.
9. E. M. Buturla, P. E. Cottrell, B. M. Grossman, and K. A. Salsburg. Finite-element analysis of semiconductor devices: The fielday program. *IBM Journal of Research and Development*, 25(4):218 –231, july 1981.
10. H. C. Elman, D. J. Silvester, and A. J. Wathen. *Finite Elements and Fast Iterative Solvers with Applications in Incompressible Fluid Dynamics*. Numerical Mathematics and Scientific Computation. Oxford University Press, 2005.
11. Timo Euler, Rolf Schuhmann, and Thomas Weiland. Polygonal finite elements. *IEEE TRANSACTIONS ON MAGNETICS*, 42(4):675–678, April 2006.
12. G. Ghione and A. Benvenuti. Discretization schemes for high-frequency semiconductor device models. *Antennas and Propagation, IEEE Transactions on*, 45(3):443 –456, March 1997.
13. I. Harari and T. J. R. Hughes. What are  $C$  and  $h$ ? Inequalities for the analysis and design of finite element methods. *Comput. Meth. Appl. Mech. Eng.*, 97:157–192, 1992.
14. P. Knobloch. On the definition of the SUPG parameter. *ETNA*, 32:76–89, 2008.
15. Kevin Kramer and W. Nicholas G. Hitchon. *Semiconductor Devices: A Simulation Approach*. Prentice Hall, Upper Saddle River, NJ 07458, 1997.
16. S.E. Laux and B.M. Grossman. A general control-volume formulation for modeling impact ionization in semiconductor transport. *Electron Devices, IEEE Transactions on*, 32(10):2076 – 2082, oct 1985.
17. Steven E. Laux and Robert G. Byrnes. Semiconductor device simulation using generalized mobility models. *IBM J. Res. Dev.*, 29:289–301, May 1985.
18. L. G. Margolin and Mikhail Shashkov. Second-order sign-preserving conservative interpolation (remapping) on general grids. *Journal of Computational Physics*, 184(1):266 – 298, 2003.
19. P. Markowich. *The stationary semiconductor device equations*. Springer Verlag, Berlin, 1986.
20. M. J. Martinez. Comparison of galerkin and control volume finite element for advection-diffusion problems. *International Journal for Numerical Methods in Fluids*, 50(3):347–376, 2006.
21. M. Mock. *Analysis of mathematical models of semiconductor devices*. Boole Press, Dublin, 1983.
22. J. C. Nédélec. Mixed finite elements in  $r^3$ . *Numerische Mathematik*, 35:315–341, 1980. 10.1007/BF01396415.
23. J. C. Nédélec. A new family of finite element methods in  $R^3$ . *Numerische Mathematik*, 50:57–81, 1986.
24. Riccardo Sacco. Exponentially fitted shape functions for advection-dominated flow problems in two dimensions. *Journal of Computational and Applied Mathematics*, 67(1):161 – 165, 1996.
25. D.L. Scharfetter and H.K. Gummel. Large-signal analysis of a silicon read diode oscillator. *Electron Devices, IEEE Transactions on*, 16(1):64 – 77, jan 1969.
26. S. Selberherr. *Analysis and simulation of semiconductor devices*. Springer-Verlag, Berlin, 1984.
27. M. Sharma and G.F. Carey. Semiconductor device simulation using adaptive refinement and flux upwinding. *Computer-Aided Design of Integrated Circuits and Systems, IEEE Transactions on*, 8(6):590 –598, June 1989.
28. C. R. Swaminathan and V. R. Voller. Streamline upwind scheme for control-volume finite elements, part i. formulations. *Numerical Heat Transfer, Part B: Fundamentals*, 22(1):95–107, 1992.
29. C. R. Swaminathan, V. R. Voller, and S. V. Patankar. A streamline upwind control volume finite element method for modeling fluid flow and heat transfer problems. *Finite Elements in Analysis and Design*, 13(2-3):169 – 184, 1993.
30. D. Z. Turner, K. B. Nakshatrala, and K. D. Hjelmstad. A stabilized formulation for the advection-diffusion equation using the generalized finite element method. *International Journal for Numerical Methods in Fluids*, 66(1):64–81, 2011.
31. Song Wang. A novel exponentially fitted triangular finite element method for an advection-diffusion problem with boundary layers. *Journal of Computational Physics*, 134(2):253 – 260, 1997.
32. Song Wang. A new exponentially fitted triangular finite element method for the continuity equations in the drift-diffusion model of semiconductor devices. *M2AN*, 33(1):99–112, 1999.